Strong structural and electronic coupling in metavalent PbS moiré superlattices

Yu Wang[1,2,†], Zhigang Song[3,†], Jiawei Wan[1,2], Sophia Betzler[1], Yujun Xie[1], Colin Ophus[4], Karen C. Bustillo[4], Peter Ercius[4], Lin-Wang Wang[1], and Haimei Zheng[1,2,*]

Affiliations:

[1]Materials Sciences Division, Lawrence Berkeley National Laboratory, Berkeley, CA 94720, USA.

[2]Department of Materials Science and Engineering, University of California, Berkeley, Berkeley, CA 94720, USA.

[3]John A. Paulson School of Engineering and Applied Sciences, Harvard University, Cambridge, MA 02138, USA

[4]National Center for Electron Microscopy, The Molecular Foundry, Lawrence Berkeley National Laboratory, Berkeley, CA 94720, USA.

[†]Contributed equally to this work.

[*]To whom correspondence should be addressed; E-mail: hmzheng@lbl.gov

Abstract

Moiré superlattices are twisted bilayer materials, in which the tunable interlayer quantum confinement offers access to new physics and novel device functionalities. Previously, moiré superlattices were built exclusively using materials with weak van der Waals interactions and synthesizing moiré superlattices with strong interlayer chemical bonding was considered to be impractical. Here using lead sulfide (PbS) as an example, we report a strategy for synthesizing moiré superlattices coupled by strong chemical bonding. We use water-soluble ligands as a removable template to obtain free-standing ultra-thin PbS nanosheets and assemble them into direct-contact bilayers with various twist angles. Atomic-resolution imaging shows the moiré periodic structural reconstruction at superlattice interface, due to the strong metavalent coupling. Electron energy loss spectroscopy and theoretical calculations collectively reveal the twist angle-dependent electronic structure, especially the emergent separation of flat bands at small twist angles. The localized states of flat bands are similar to well-arranged quantum dots, promising an application in devices. This study opens a new door to the exploration of deep energy modulations within moiré superlattices alternative to van der Waals twistronics.

Introduction

Recently, moiré superlattices have been synthesized by stacking two layers of two-dimensional (2D) materials with relative twist angles[9,10], in which the long-range superlattice potentials from interlayer interactions can create quantum confinement in each layer. Quantum confinement in moiré superlattices can slow down or localize electrons, providing a tunable platform for studying strongly correlated physics[1,2], such as superconductivity[3,4], Mott insulators[5], and interacting topological insulators[6,7]. In the moiré superlattices, the twisting topology determines the 2D quantum confinement and it offers an additional degree of freedom to modulate the electronic structure, usually referred to as twistronics[11,12]. So far, all 2D moiré superlattices are synthesized using van der Waals (vdW) materials[8], such as graphene and transition-metal dichalcogenide, where the two layers of materials are coupled through vdW interactions. Twistronics based on these vdW materials has attracted great interest in various fields, ranging from physics[13–20] to materials science[9,21–23], and chemistry[24,25]. Different from materials coupled by chemical bonding at an interface, such as conventional semiconductor heterostructures, vdW twistronics have reduced strength in modulating the electronic structures due to the weak interlayer coupling, although strong coupling in twistronics is desired.[?,?] Most of the experimental observations of exotic electronic properties, especially those associated with electron transport, are realized at extremely low temperatures[1,2,5,?–7]. To increase the electronic modulation imposed by moiré superlattice, one approach is to replace the vdW interactions with strong chemical bonding such as covalent, ionic, or metavalent bonding.

Achieving strong quantum confinement in moiré superlattices by chemical bonding will pave a way to fabricating a new class of materials for beyond-vdW twistronics[?], and it may also shed light on some challenging issues in other systems. For example, strongly coupled moiré superlattices can be structurally and functionally similar to an array of quantum dots[26], offering an alternative route to super-crystals[27] by avoiding the notorious issue of connection defects formed during quantum dot self-assembly[28]. Moreover, the energy bands near the Fermi level in moiré patterns can be flattened due to the strong modulation, which may trap electrons in individual "quantum-dot" potentials upon suitable doping, leading to Wigner crystallization[29,?,?]. Thus, creating strongly coupled moiré superlattices through chemical bonding combines the strengths of two fields: the tunable confinement of 2D moiré superlattices and the strong coupling in conventional semiconductor heterostructures. Since moiré superlattices cannot be achieved using conventional semiconductor synthesis methods, e.g., epitaxial growth[9,30], it is unclear whether it is possible to synthesize chemically bonded moiré superlattices.

Here, we use PbS as a model system to demonstrate a strategy for constructing moiré superlattices with strong interlayer coupling through metavalent bonding. Such beyond-vdW moiré superlattices are obtained for the first time through chemical synthesis. Strong interfacial coupling of the superlattice is revealed through atomic-resolution imaging, and the giant electronic

modulation of moiré pattern is validated through the combination of electron energy loss spectroscopic analysis and theoretical calculations.

Results and Discussion

Conceptual discussion of metavalent moiré superlattices

We first describe theoretically why metavalent moiré superlattices can give rise to stronger coupling effects than vdW moiré superlattices. As shown in Fig. 1a, bulk PbS has a rock-salt crystal structure and features an unconventional chemical bonding between Pb and S atoms, namely metavalent bonding, in which the valence electrons are delocalized to an extent between covalent and metallic bonding[25]. This metavalent Pb–S bonding is much stronger than vdW interactions[9], and it can be used as the interlayer interaction to construct strongly coupled PbS moiré superlattices if one can assemble ultra-thin 2D PbS nanosheets with pristine surfaces into twisted bilayers. This methodology may be further generalized to obtain new moiré superlattices coupled by other types of interfacial chemical bonding, for example, MXene[31] moiré superlattices coupled by metallic bonding, perovskite[32] moiré superlattices coupled by ionic bonding, and twisted bilayers of metal–organic frameworks[33] coupled by mixed interactions.

PbS moiré supercells with small commensurate angles have a tetragonal symmetry (Fig. 1b), in which two types of interfacial atoms stacked into four general configurations: Pb on Pb (marked as AA), Pb on S (marked as AB), the middle point (MP) between AA and AB, and the diagonal point (DP) between two AB positions. In small-angle twisted bilayers, each stacking configuration can be approximated by small unit cells consisting of laterally shifted bilayers, in which the shift coordinates are scaled by x and y in the unit of cell size (Fig. 1c). Therefore, the AB, AA, MP, and DP configurations correspond to the (x, y) of $(0, 0)$, $(0, 0.5)$, $(0, 0.25)$, and $(0.25, 0.25)$, respectively, and other configurations between the four extrema can be constructed with continuous (x, y) shift.

Density-functional theory (DFT) calculations on the created structures (detailed in Supplementary Text S1) suggest that different stacking configurations can lead to deep modulations of interfacial reconstruction and electronic properties. Fig. 1d,e shows the changes of interlayer distance and free energy as functions of lateral interlayer shift. The surface plot regarding either interlayer distance or free energy has the maxima at AA spots and the minima at AB spots. The difference between the maximum and minimum interlayer distance is as large as 0.6 Å, implying a possible structural reconstruction at the interface of a small-angle twisted superlattice.

Maximal free energy fluctuation in the real space is defined as moiré potential[17]?, which is an important indicator of the strength of energy modulation for a given moiré superlattice. We estimate the moiré potential of PbS and other 2D materials by calculating the largest free energy difference among all possible stacking configurations using approximate small unit cells. Fig. 1f shows the calculated moiré potentials of various materials, including the reported vdW
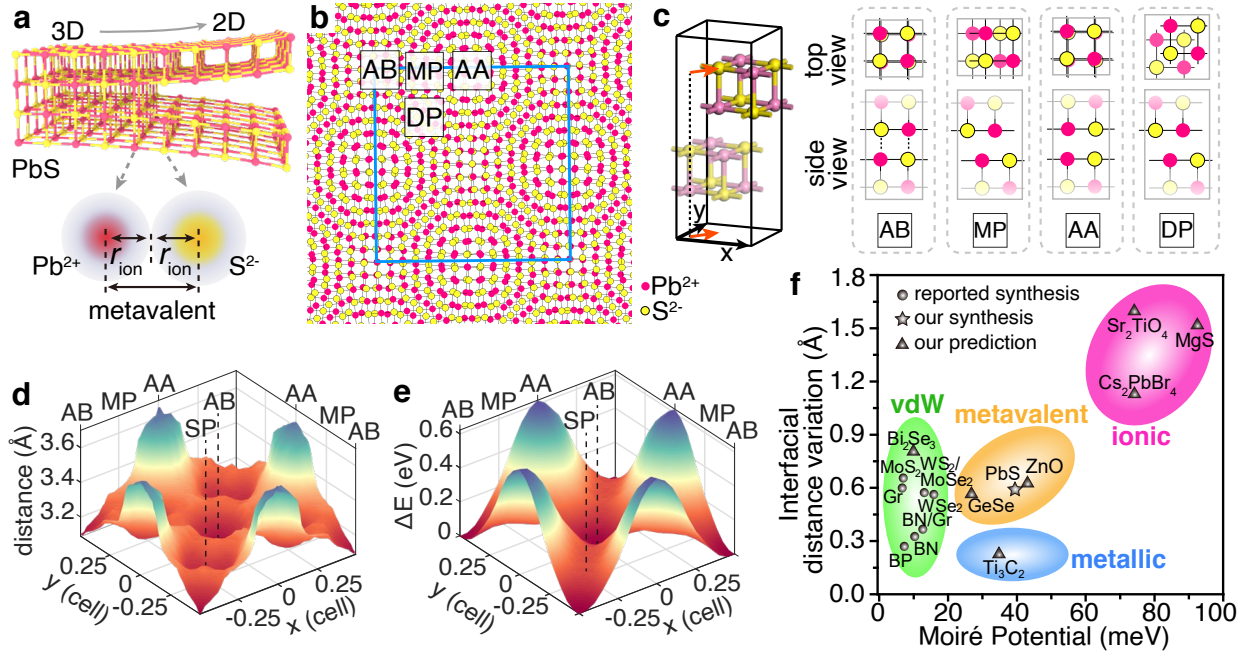
Fig. 1 | Structure and strong coupling of PbS moiré superlattice. **a**, 3D and the cleaved 2D structures of PbS rock-salt crystal, emphasizing the metavalent interaction in all directions. **b**, Different local atomic alignments occur in a PbS moiré superlattice with a twist angle of 8°. Blue square marks the moiré unit-cell. Four representative stacking configurations are highlighted as Pb on Pb (AA), Pb on S (AB), middle point (MP), and diagonal point (DP). **c**, Illustration of laterally shifting two PbS nanosheets for creating different stacking configurations. Top views and side views of representative structures are exemplified. **d,e**, DFT calculations of the structures created according to panel (c) showing the interfacial distance (d) and the free energy change (e) upon the bilayer lateral shift. **f**, DFT calculations on varieties of moiré superlattices, including the reported vdW superlattices, the metavalent PbS synthesized in this work, and our predictions of other chemically bonded superlattices. The results show their moiré potential and the largest interfacial distance variation among different stacking configurations.

superlattices, the metavalent PbS synthesized in this work, and our predictions of other chemically bonded superlattices. The moiré potential of PbS is 40 meV per atom, more than twice of the reported vdW superlattices. Generally, chemical bonding (e.g., metallic, metavalent, and ionic bonding) leads to much deeper energy modulation compared to vdW interactions. The deep energy modulation can localize electrons in the high-symmetry points with local energy extrema, providing an array of identical quantum-dot-like potentials[26,27]. Until now, the properties of the chemically bonded moiré superlattices and their structural stability remain unknown due to the lack of a synthesis strategy.

Synthesis and characterization of PbS moiré superlattices

We use metavalent PbS as a model system of beyond-vdW moiré superlattices to assess the feasibility of achieving the predicted modulation of electronic structures. Ultra-thin PbS nanosheets have been previously synthesized in organic low-polar solvents[34], in which the interaction between the solvent-phobic PbS core and the long-alkyl-chain ligands is designed to

be strong to guide asymmetric growth and stabilize the formed nanocrystals. However, the strong core–ligand interaction also leads to difficulty in ligand removal, and the ligands prevent direct metavalent bonding between two nanosheets[34]. To overcome this dilemma, we developed an aqueous synthesis strategy employing two surfactant ligands that have adequate solubility and bind moderately with the inorganic core. The schematic in Fig. 2a shows that Pb^{2+} and S^{2-} precursors and two organic ligands (i.e., hexylamine and dodecyl sulfate) in an acidic aqueous solution at 80°C for 20 min produce ligand-capped ultra-thin PbS nanosheets (Supplementary Method S1). TEM imaging and statistics (Supplementary Fig. S1) show that the nanosheets have a rectangular shape with an average width and length of around 40 nm × 200 nm. The synthetic mechanism is discussed in Supplementary Text S2. Due to the high polarity of the PbS surfaces, high-polar solvents (such as water) are required to remove the ligands. In this synthesis method, both ligands can be readily removed by washing with dilute basic and acidic aqueous solutions alternatively, in contrast to the long-alkyl-chain ligands used in conventional synthesis. After ligand removal, the naked PbS nanosheets are immediately drop-casted, allowing the assembly of moiré superlattices through solvent evaporation.

Aberration-corrected transmission electron microscopy (TEM) imaging (Fig. 2b) and the zoomed-in portion from the yellow box (Fig. 2c) with corresponding image simulation (Fig. 2c inset) show that the as-synthesized nanosheets have a rock-salt structure with {001} surfaces and {110} edges. Energy-dispersive X-ray spectroscopy confirms that the moiré superlattice consists of Pb and S atoms at a molar ratio of 1:1 (Supplementary Fig. S2). Bilayer moiré superlattices with various twist angles are observed at low magnification due to the presence of moiré fringes (Fig. 2d,e). A fast Fourier transform (FFT) of a representative moiré superlattice TEM image shows the expected pattern of two rotated sets of spatial frequencies corresponding to the structure of each sheet (Fig. 2e). In the enlarged images (bottom panels of Fig. 2e), the two red dots correspond to the (200) d-spacing of two individual sheets, the set of blue dots correspond to the d-spacings of the moiré pattern, and the orange dots correspond to the addition of the spatial frequencies from individual sheets and the moiré pattern. The theoretical relationship between the FFT pattern of an individual nanosheet and that of a moiré pattern is illustrated in Fig. 2f inset, and accordingly, the moiré d-spacing can be calculated by:

$$d_{\mathrm{m}}(200) = \frac{d_{\mathrm{rs}}(200)}{2 \cdot \sin(\theta/2)} \tag{1}$$

where θ is the twist angle; d_{m} and d_{rs} are the (200) d-spacing of the moiré cell and the rock-salt cell, respectively. In addition, the moiré d-spacing can also be directly measured from high-resolution TEM images for a variety of twist angles, verifying the calculated results from Eq. 1 as plotted in Fig. 2f.

Fig. 2g–i and Supplementary Fig. S3 show atomic-resolution TEM images and corresponding image simulations (blue images; see Supplementary Method S2) of moiré superlattices with various twist angles. For smaller twist angles, the (quasi-) unit cell of the moiré pattern is more
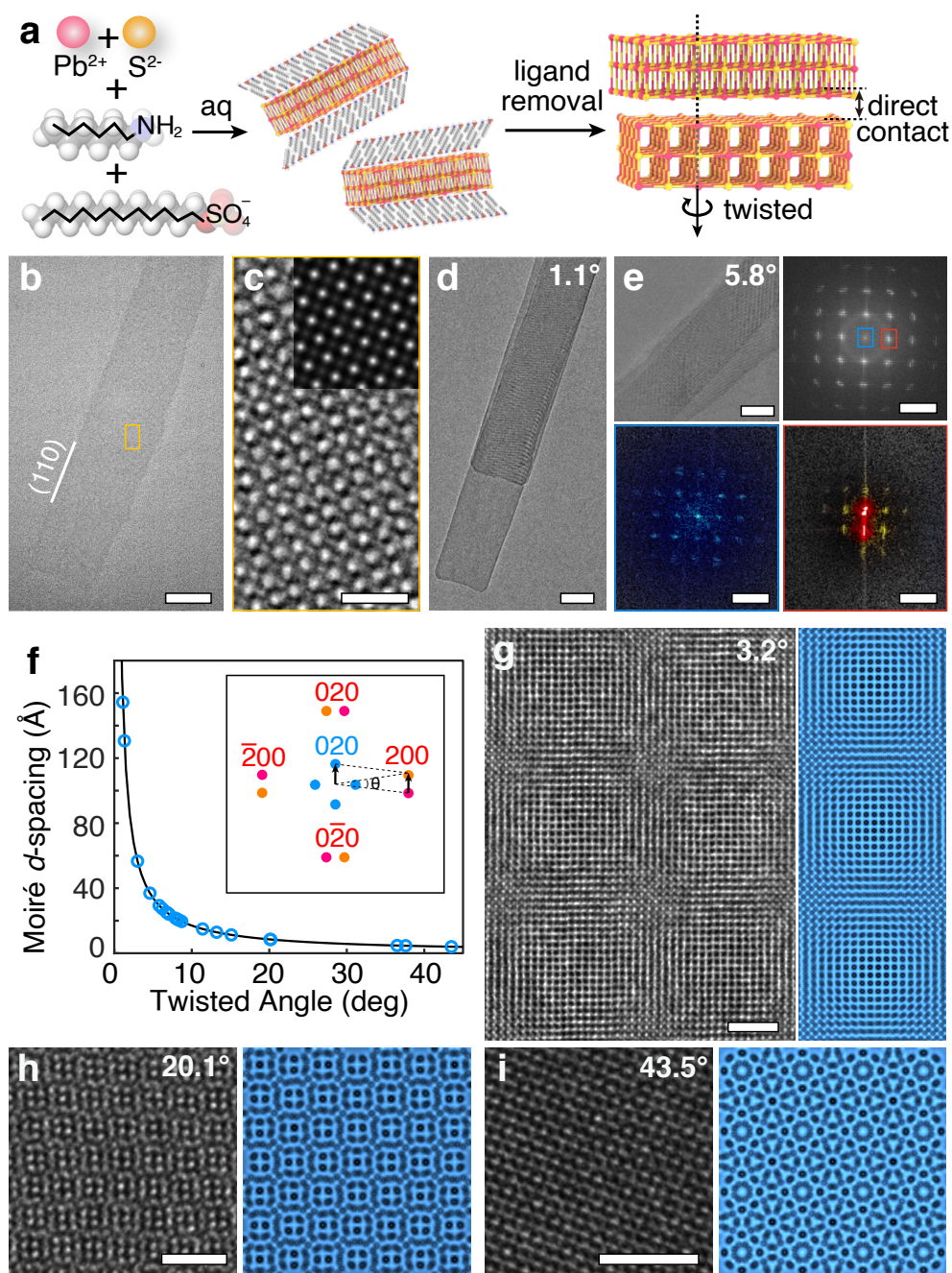
Fig. 2 | Synthesis and TEM characterizations of PbS moiré superlattices. **a**, Schematics of synthetic procedures. **b**, Low magnification TEM image of a single ultra-thin PbS nanosheet. **c**, Atomic-resolution image of the boxed area in panel b with an inserted simulation of TEM image. **d**, TEM image of a bilayer moiré superlattice with a 1.1° twist angle. **e**, TEM image (top-left) and FFT pattern (top-right) of a bilayer moiré superlattice with a 5.8° twist angle. Two bottom panels show the enlarged details of the FFT pattern, in which blue dots indicate moiré spatial frequencies, red dots indicate the (200) spatial frequencies of two individual rock-salt nanosheets, and orange dots indicate the emerged pattern from moiré pattern and individual rock-salt patterns. **f**, Theoretical (black curve) and observed (green hollow dots) relationship between moiré d-spacing (200) and twist angles. Inset shows the relationship between moiré spatial frequencies (green) and two sets of individual rock-salt spatial frequencies (red and orange). **g–i**, Atomic-resolution TEM images and corresponding simulated images (false coloured) of bilayer moiré superlattices with a variety of twist angles. Scale bar: b, 30 nm; c, 1 nm; d, 100 nm; e, 30 nm (top left), 5 nm^{-1} (top right), 0.5 nm^{-1} (bottom two); g–i, 2 nm.

6

obvious, and the superlattice appears as an array of identical quantum dots. For example, the moiré superlattice with a 3.2° twist angle (measured by the rotation angle of FFT spots) consists of periodic AA/AB regions arranged in square symmetry with DP regions filled in the diagonal positions (Fig. 2g), resembling an epitaxially fused superlattice of 5~6 nm PbS quantum dots[28]. At a large twist angle close to 45°, the moiré superlattice resembles 2D octagonal quasicrystals (Fig. 2i), showing an approximate C_8 symmetry in TEM image and reflecting the S_8 symmetry of octagonal quasicrystals.

Structural analysis of moiré superlattice interface

Fig. 3a shows the TEM image along the basal plane (side-view) of a moiré superlattice composed of three PbS sheets (labelled as S1, S2, and S3). The three sheets have a consistent thickness, approximately 3.0 nm, and consist of 10 (002) planes. Neighbouring sheets (S1–S2 or S2–S3) are in direct contact with 3 Å interfacial spacing and no trace of ligands at interface. For comparison, a bilayer with even one interfacial ligand residue would appear rather different, showing a larger interfacial distance over 5 Å (Supplementary Fig. S4). The clear interface between PbS sheets suggests the efficiency of the as-described ligand removal method.

Note that, S1 and S3 are deformed beyond the right end of S2, indicating strong interlayer metavalent interactions and large deformability of naked PbS at the sub-10-nm scale[35]. This large deformability of uncoupled nanosheets is consistent with the self-rolling behaviour of individual naked nanosheets in the solution phase (Supplementary Text S3). Additionally, this also suggests that forming superlattices is an effective way to stabilize the naked nanosheets.

Further scrutiny of the side-view image in Fig. 3b reveals that S1 is oriented along a [110] axis regarding the viewing direction based on the observed elongated hexagonal pattern, whereas S2 is tilted away from a low-index zone axis. This indicates that the sheets are rotated around the basal plane regarding one another, confirming the formation of moiré superlattices with direct interlayer contact. We further measured the lattice spacings in the superlattice at different X locations in real space based on TEM image simulations and the recognition of the image peak positions, as detailed in Supplementary Text S4. The right graph in Fig. 3b shows an example at X = 79 Å, where the (002) spacings are approximate to 3.0 Å (similar to that in the bulk crystal) for the inner layers inside each sheet, but become slightly larger at the S1–S2 interface. We select two internal interlayers in each sheet (labelled as Internal 1 and 2) and the S1–S2 interface representative interlayers, and examine their interlayer spacing at different X locations. As shown in Fig. 3c, the spacings of Internal 1 and 2 are consistent to *c.a.* 3.0 Å with small fluctuation less than 0.1 Å, however, both the mean value (3.35 Å) and the fluctuation (over 0.2 Å) of interfacial spacing are considerably larger. Moreover, the fluctuation of interfacial spacing exhibits a periodicity that matches with the theoretical moiré periodicity of bilayer superlattice with a 11.5° twist angle. We simulate the side-view image of the theoretically optimized 11.5° twist superlattice and calculate the interfacial spacing in the simulated image (Fig. 3d). There is indeed a considerable interfacial

spacing fluctuation in the simulated image that matches with the theoretical moiré periodicity. The experimental and theoretical structural analysis jointly suggests the structural reconstruction at superlattice interface and its correlation to moiré periodicity.

Twist angle-dependent electronic states of moiré superlattices

We employ monochromated electron energy loss spectroscopy (EELS) in an aberration-corrected scanning TEM (STEM) to investigate the electronic excitation of moiré superstructures as a function of twist angle. Owing to the advantage of the latest direct detection camera and the large absorption efficiency of PbS, the low-loss spectra in the exciton region exhibit high signal-to-noise ratios (Supplementary Fig. S5). Fig. 4a shows the overview images of two representative superlattices with twist angles of 1.3° and 3.0° and the corresponding EELS scanning profiles. Other superlattices that were measured have larger twist angles 4.6°, 12°, and 35°. Because all moiré superlattices were measured in one experiment with identical conditions, we can compare the thickness of individual sheets from the scattering intensity from non-overlapping regions with only a single sheet in projection. We find that all individual nanosheets in the moiré superlattices have a similar thickness with less than 10% difference.

The integrated spectra of the double-layer regions with various twist angles are plotted in Fig. 4b, and the peak locations are extracted in Fig. 4c. These plots show that the spectral peak slightly shifts to lower energy as the twist angle decreases from 35.3° to 3.0°, but the peak energy dramatically decreases from 3.0° to 1.3°.

Features in low-loss EEL spectra arise due to inter-band excitation and intra-band transitions in a similar way to optical spectra[36,37], which are qualitatively reflective of the electronic excitation or the bandgap. To understand the abrupt EELS peak change at small twist angle, we perform direct self-consistent calculations by constructing large moiré unit cells (up to 4360 atoms) with commensurate angles (Supplementary Text S1). The density of states (DOS) of the moiré cells with twist angles ranging from 4.47° to 43.6° are shown in Fig. 4d, and the corresponding bandgaps are plotted in Fig. 4e. For superlattices with a twist angle larger than 10.4°, the bandgap fluctuates around a constant. However, the bandgap drops rapidly as the twist angle decreases from 10.4° to smaller angles (Fig. 4e). This calculated relationship between bandgap and twist angle, especially the sharp drop of bandgap at a small angle, is in good agreement with our EELS experiments (Fig. 4c). The experimental and theoretical results collectively suggest that the band structure of metavalent moiré superlattices, is highly dependent on the twist angle, especially at small twist angles.

Band structure calculations of PbS moiré superlattices

In addition to the twist angle-dependent bandgap, the DFT calculations of band structures reveal the emergent separation of electronic states of superlattices at small twist angles (Fig. 5a,b and Supplementary Fig. S6). As the twist angle of a superlattice falls below 10°, the bands become
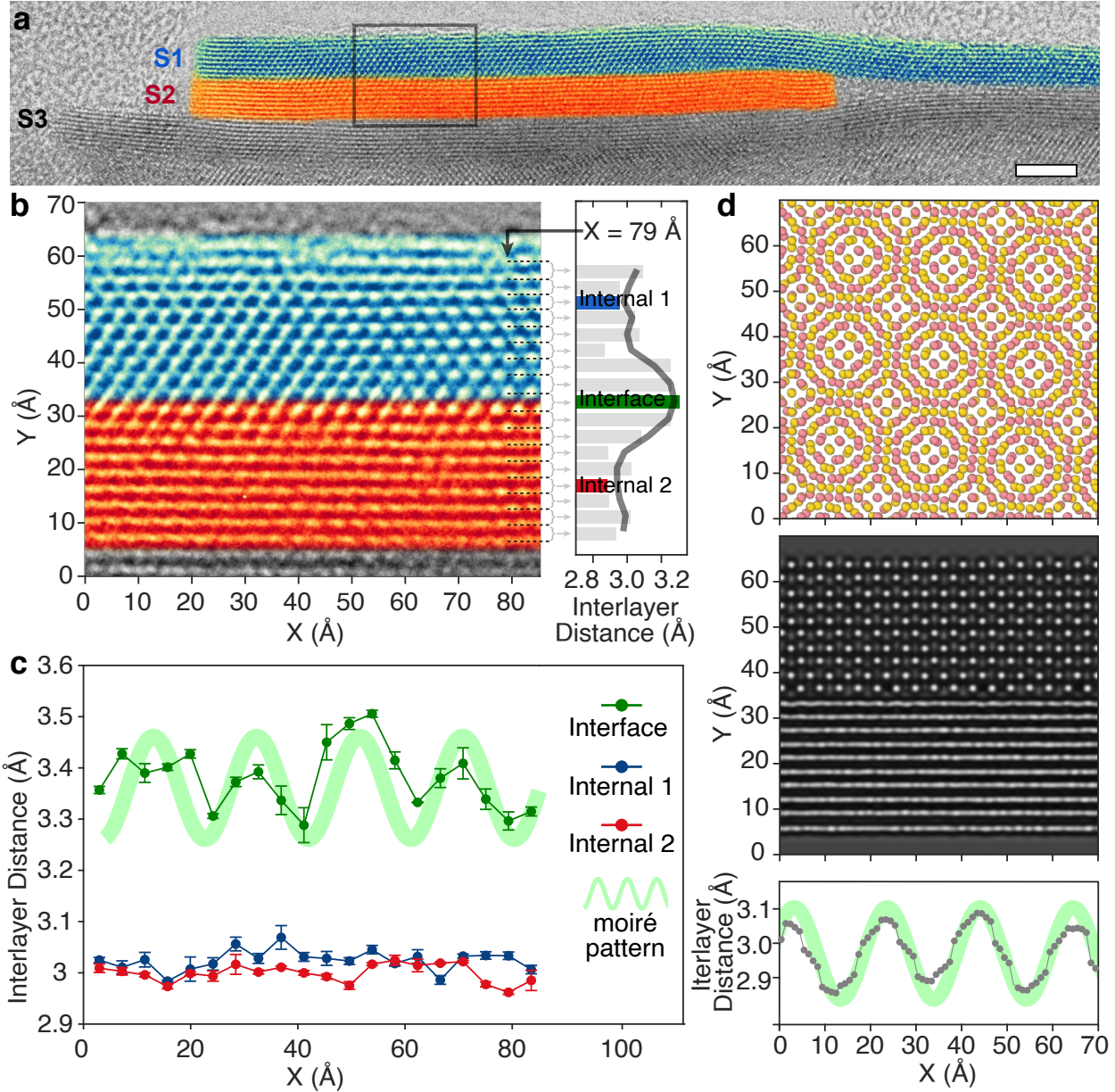
Fig. 3 | Structural analysis of moiré superlattice interface. **a**, Side view of a moiré superlattice composed of three sheets, S1, S2, and S3. S1 and S2 are false-coloured for clarity. Scale bar, 5 nm. **b**, Higher-resolution image of the boxed region in panel a and the demonstration of measuring interlayer distances. The Y positions of each layer (marked by dash lines) are evaluated by finding the brightest dots/strips in the image at the section of X = 79 Å, and the interlayer distances are calculated as the difference of neighbouring Y positions (marked by brackets and arrows). Two internal interlayers in each sheet and the interface of S1 and S2 are highlighted by blue, red, and green, respectively, as representative interlayers for further analysis in panel c. **c**, Interlayer distance fluctuation by measuring three representative interlayers at different X locations. Error bars indicate the standard deviation of measurements using three different sampling widths of 4, 6, and 8 Å. Thick green line shows the moiré periodicity of the bilayer superlattice with an 11.5° twist angle. **d**, Theoretically optimized atomic structure (up), simulated side-view image (middle), and calculated interfacial distance fluctuation (bottom, gray dots) of an 11.5° twist superlattice. Moiré periodicity (thick green line) for comparison.

9

narrower due to the quantum containment of the moiré pattern, and bands near the Fermi level begin to separate from the deep and high-energy states. For example, in the case of 3.47°, the bands near the Fermi level, especially the conduction band, become extremely flat (Fig. 5a,b). This emergent separation of electronic states is probably the reason of the observed peak split in the EELS spectrum at 1.3° (Fig. 4b). Supplementary calculations (Supplementary Fig. S6) show that the separation of moiré bands, which reflects the modulation effect by moiré pattern, becomes weaker as nanosheets become thicker. This separation of moiré bands, which reflects the modulation effect by moiré pattern, becomes weaker as nanosheets become thicker. This thickness-dependent of modulation indicates the value of synthesizing ultra-thin free-standing nanosheets, stimulating future developments in the chemical and/or physical syntheses of ultra-thin beyond-
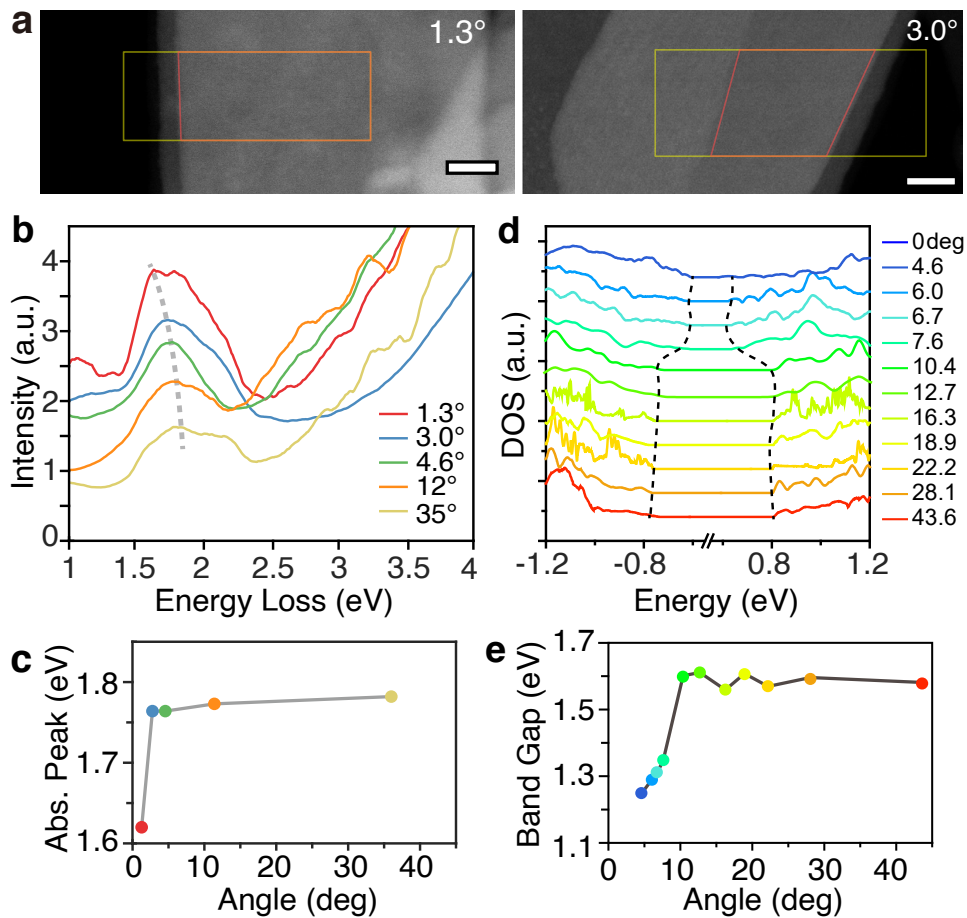

Fig. 4 | Twist angle-dependent STEM-EELS and electronic states of moiré superlattices. **a**, Overview images of two representative superlattices with twist angles of 1.3° and 3.0°. Yellow and red boxes mark the scanning regions and bilayer regions for STEM-EELS integration, respectively. Scale bar, 20 nm. **b**, Energy loss spectra of the bilayer regions of moiré superlattices with a variety of twist angles. Energy dispersion of all spectra is 9 meV/pixel. **c**, Change of spectral peak upon twist angles extracted from panel d. **d**, Direct calculation of the density-of-states of commensurate moiré superlattices with a variety of twist angles. Black dashed lines connect the positions of first valence or conduction band for each structure. **e**, Bandgap change upon twist angles extracted from panel d.

vdW nanosheets and their strongly coupled moiré superlattices.

Furthermore, these separated moiré bands at small twist angles are highly spatially localized. Fig. 5d shows the corresponding wave functions of the conduction and valence bands, which are localized at AB and AA spots, respectively, with diameters of a few nanometres. This also indicates that the PbS moiré superlattice not only structurally resembles but also functionally mimics a well-arranged array of quantum dots with separate energy levels and electron orbitals. Our additional calculation (Supplementary Text S5) suggests that the strong metavalent modulation by the moiré pattern may lead to emergent opto-electronic properties in valleytronics, such as valley-dependant optical selection rules.
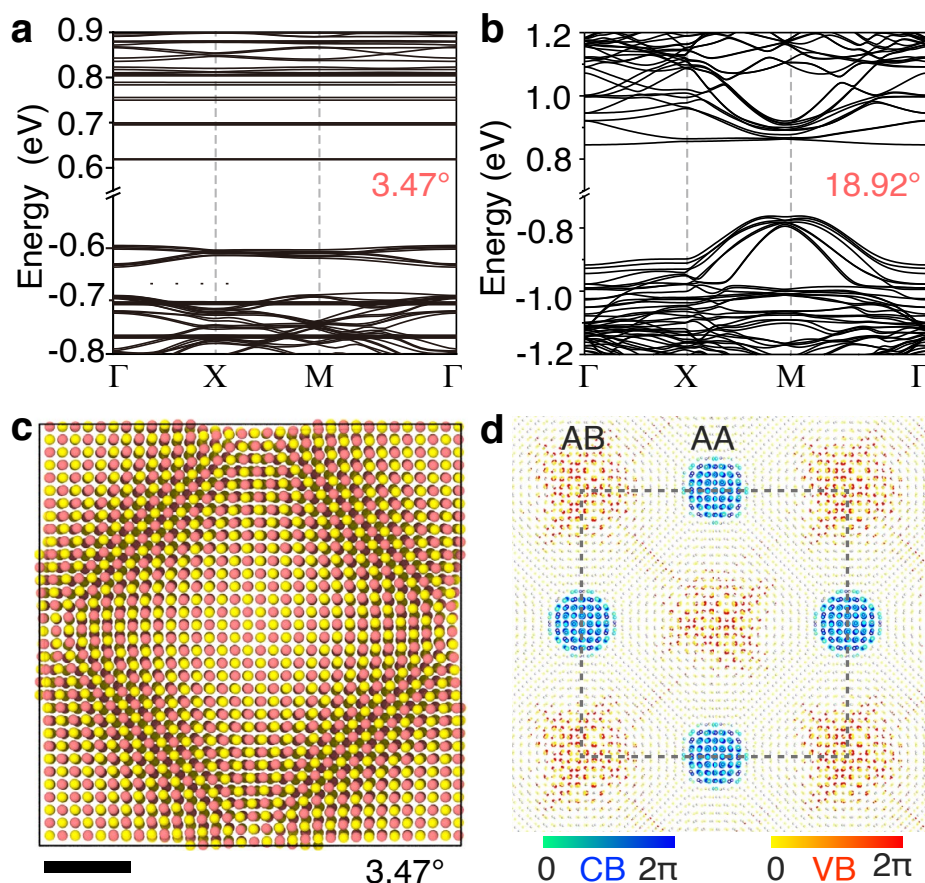

Fig. 5 | DFT calculations of the electronic localization. **a,b** Calculated band structures of the superlattices with twist angles of 3.47° and 18.92°. **c**, Theoretically optimized moiré cell of the superlattice with a twist angle of 3.47°. **d**, Charge density of valence band (VB) and conduction band (CB). Colour is coded by the phase of wave function. Moiré cell is marked by the dashed line.

Conclusion

We have established an approach to introduce strong metavalent interlayer interactions into moiré superlattices. Our synthesis strategy and findings on the chemically bonded moiré superlattices

extend the current twistronics. Combining structural analysis, EELS measurements, and DFT calculations, we demonstrate that strong moiré modulation at a small twist angle can lead to considerable structural reconstruction and electronic renormalization. This study provides a route to arrays of identical "quantum-dot" potentials by achieving deep energy modulation through metavalent interactions, providing an alternative platform for spatially variant electronic and opto-electronic properties. We anticipate that further experimental and theoretical studies on beyond-vdW moiré superlattices will find more types of interlayer interactions that may result in strong electronic coupling, strong correlation, and realizing tunable emergent quantum properties.

Data availability

The data that support the findings of this study are available from the corresponding authors on reasonable request.

References

[1] Tang, Y. *et al.* Simulation of Hubbard model physics in WSe_2/WS_2 moiré superlattices. *Nature* **579**, 353–358 (2020).

[2] Lu, X. *et al.* Superconductors, orbital magnets and correlated states in magic-angle bilayer graphene. *Nature* **574**, 653–657 (2019).

[3] Cao, Y. *et al.* Unconventional superconductivity in magic-angle graphene superlattices. *Nature* **556**, 43–50 (2018).

[4] Arora, H. S. *et al.* Superconductivity in metallic twisted bilayer graphene stabilized by WSe_2. *Nature* **583**, 379–384 (2020).

[5] Cao, Y. *et al.* Correlated insulator behaviour at half-filling in magic-angle graphene superlattices. *Nature* **556**, 80–84 (2018).

[6] Nuckolls, K. P. *et al.* Strongly correlated Chern insulators in magic-angle twisted bilayer graphene. *Nature* **588**, 610–615 (2020).

[7] Chen, G. *et al.* Tunable correlated Chern insulator and ferromagnetism in a moiré superlattice. *Nature* **579**, 56–61 (2020).

[8] Carr, S., Fang, S. & Kaxiras, E. Electronic-structure methods for twisted moiré layers. *Nat. Rev. Mater.* **5**, 748–763 (2020).

[9] Liu, Y., Huang, Y. & Duan, X. Van der Waals integration before and beyond two-dimensional materials. *Nature* **567**, 323–333 (2019).

[10] Bediako, D. K. *et al.* Heterointerface effects in the electrointercalation of van der Waals heterostructures. *Nature* **558**, 425–429 (2018).

[11] Ribeiro-Palau, R. *et al.* Twistable electronics with dynamically rotatable heterostructures. *Science* **361**, 690–693 (2018).

[12] Hu, G. *et al.* Topological polaritons and photonic magic angles in twisted α-MoO$_3$ bilayers. *Nature* **582**, 209–213 (2020).

[13] Dean, C. R. *et al.* Hofstadter's butterfly and the fractal quantum hall effect in moiré superlattices. *Nature* **497**, 598–602 (2013).

[14] Jiang, Y. *et al.* Charge order and broken rotational symmetry in magic-angle twisted bilayer graphene. *Nature* **573**, 91–95 (2019).

[15] Uri, A. *et al.* Mapping the twist-angle disorder and landau levels in magic-angle graphene. *Nature* **581**, 47–52 (2020).

[16] Sunku, S. S. *et al.* Photonic crystals for nano-light in moiré graphene superlattices. *Science* **362**, 1153–1156 (2018).

[17] Tran, K. *et al.* Evidence for moiré excitons in van der Waals heterostructures. *Nature* **567**, 71–75 (2019).

[18] Alexeev, E. M. *et al.* Resonantly hybridized excitons in moiré superlattices in van der Waals heterostructures. *Nature* **567**, 81–86 (2019).

[19] Seyler, K. L. *et al.* Signatures of moiré-trapped valley excitons in MoSe$_2$/WSe$_2$ heterobilayers. *Nature* **567**, 66–70 (2019).

[20] Sharpe, A. L. *et al.* Emergent ferromagnetism near three-quarters filling in twisted bilayer graphene. *Science* **365**, 605–608 (2019).

[21] Sutter, P., Wimer, S. & Sutter, E. Chiral twisted van der Waals nanowires. *Nature* **570**, 354–357 (2019).

[22] Rhodes, D., Chae, S. H., Ribeiro-Palau, R. & Hone, J. Disorder in van der Waals heterostructures of 2D materials. *Nat. Mat.* **18**, 541–549 (2019).

[23] Weston, A. *et al.* Atomic reconstruction in twisted bilayers of transition metal dichalcogenides. *Nat. Nanotech.* **15**, 592–597 (2020).

[24] Dong, R., Zhang, T. & Feng, X. Interface-assisted synthesis of 2D materials: Trend and challenges. *Chem. Rev.* **118**, 6189–6235 (2018).

[25] Kooi, B. J. & Wuttig, M. Chalcogenides by design: Functionality through metavalent bonding and confinement. *Adv. Mater.* **32**, 1908302 (2020).

[26] Song, Z., Sun, X. & Wang, L. Switchable asymmetric moiré patterns with strongly localized states. *J. Phys. Chem. Lett.* **11**, 9224–9229 (2020).

[27] Zhang, C. *et al.* Interlayer couplings, Moiré patterns, and 2D electronic superlattices in MoS$_2$/WSe$_2$ hetero-bilayers. *Sci. Adv.* **3**, e1601459 (2017).

[28] Whitham, K. *et al.* Charge transport and localization in atomically coherent quantum dot solids. *Nat. Mat.* **15**, 557–563 (2016).

[29] Wigner, E. Effects of the electron interaction on the energy levels of electrons in metals. *Trans. Faraday Soc.* **34**, 678–685 (1938).

[30] Oh, M. H. *et al.* Design and synthesis of multigrain nanocrystals via geometric misfit strain. *Nature* **577**, 359–363 (2020).

[31] Naguib, M., Mochalin, V. N., Barsoum, M. W. & Gogotsi, Y. 25th anniversary article: MXenes: a new family of two-dimensional materials. *Adv. Mater.* **26**, 992–1005 (2014).

[32] Ji, D. *et al.* Freestanding crystalline oxide perovskites down to the monolayer limit. *Nature* **570**, 87–90 (2019).

[33] Wu, M. *et al.* Conetronics in 2D metal-organic frameworks: double/half Dirac cones and quantum anomalous Hall effect. *2D Mater.* **4**, 015015 (2016).

[34] Schliehe, C. *et al.* Ultrathin PbS sheets by two-dimensional oriented attachment. *Science* **329**, 550–553 (2010).

[35] Wang, Y. *et al.* Dynamic deformability of individual PbSe nanocrystals during superlattice phase transitions. *Sci. Adv.* **5**, eaaw5623 (2019).

[36] Hage, F. S. *et al.* Nanoscale momentum-resolved vibrational spectroscopy. *Sci. Adv.* **4**, eaar7495 (2018).

[37] Gogoi, P. K. *et al.* Layer rotation-angle-dependent excitonic absorption in van der Waals heterostructures revealed by electron energy loss spectroscopy. *ACS Nano* **13**, 9541–9550 (2019).

Acknowledgements

Author contributions

Y.W. conceived and H.Z. supervised this project. Y.W. and J.W. designed and performed the synthesis. Y.W. performed TEM imaging with contribution from Y.X. P.E. and Y.W. conducted EELS measurement with contribution from S.B. and K.B. C.O. provided the code for analysing side-view images. Y.W. analysed all experimental data. Z.S. performed theoretical analysis under the supervision of L.-W.W. Y.W., Z.S., and H.Z. wrote the manuscript with input from all authors.

Competing interests

The authors declare no competing interests.

Supplementary information

Supplementary Figs. S1–S5, Supplementary Methods, and Supplementary Text S1–S5 are available for this paper at https://doi.org/.